WELDING RESEARCH

SUPPLEMENT TO THE WELDING JOURNAL, NOVEMBER, 1981
Sponsored by the American Welding Society and the Welding Research Council

The Fracture Toughness of Steel-Aluminum Deformation Welds

Kirkendal porosity, rather than intermetallic compounds, is found to be the cause of embrittlement in steel-aluminum welds

BY C. E. ALBRIGHT

Introduction

The welding of aluminum to steel is becoming increasingly attractive as the use of aluminum and its alloys becomes more and more commonplace (Ref. 1-3). There are, however, two major problems associated with aluminum-steel weldments. The first is the extreme susceptibility of such joints to galvanic corrosion due to their large differences in galvanic solution potentials (Ref. 6). The second is the embrittlement that can occur in the welded joint.

This paper does not address itself to the problem of galvanic corrosion. Instead, it focuses on the problem of embrittlement which can be defined further as follows: During the welding of aluminum to steel or during postweld heat treatment or high temperature service, the aluminum may react with the iron in the steel to form intermetallic compounds. These compounds form at the steel-aluminum interface and can cause extreme embrittlement of the joint. Since the reaction is much more rapid in liquid phases than in solid phases, at the present time aluminum-steel joints made by fusion welding or aluminum brazing techniques are extremely brittle. (Ref. 3, 5).

The problem is not limited to the aluminum-iron binary system. The embrittlement phenomenon has been observed in a number of systems that form intermetallic compounds (Ref. 6). McEwan and Milner did the first detailed work on intermetallic compound formation causing embrittlement of dissimilar metal solid phase welds (Ref. 6). They demonstrated that a thin layer of an intermetallic compound would not affect the ductility of the joint, but that a thick layer in the same joint would cause extreme embrittlement. The critical thickness to cause embrittlement varied with the ductility of the intermetallic compound; brittle compounds like those in iron-aluminum systems had critical thicknesses so small that McEwan, *et al.* could not resolve the layers with the optical microscope, while ductile compounds like those in the aluminum-silver system did not produce any embrittlement in specimens with intermetallic layer thicknesses up to 40 μm.

Fracture toughness testing of dissimilar metal joints is difficult because few analytical solutions exist for the calculation of K, the stress intensity, in composite specimens. In such cases, it is often convenient to perform a compliance calibration using the relationship between the stored elastic strain energy in the specimen and the crack extension force. Mostovoy and Ripling used this compliance calibration approach to successfully measure the fracture toughness of epoxy adhesive joints (Ref. 7). A similar technique is applied in this study.

The purpose of this study was to investigate joint toughness as a function of intermetallic compound morphology in the aluminum-steel system. By employing fracture toughness testing, a materials property characteristic of the fracture process is obtained. Scanning electron microscopy and metallography are used to complement the fracture toughness testing, so that the location of the fracture event can be identified with respect to the various joint interfaces.

Experimental Procedure

Welding was performed by compressing a pure aluminum cylinder between two ground and polished steel surfaces, and forging the aluminum to a very thin sheet between the steel surfaces. This method of preparation provides the following advantages:

1. Since the steel is much stronger than the pure aluminum, this method provides a very controlled method of deforming the aluminum with deformation being confined to the aluminum.

2. High pressures are developed in the aluminum due to elastic constraint pro-

Based on paper sponsored by the Aluminum Alloys Committee of the Welding Research Council for presentation at the 61st AWS Annual Meeting held in Los Angeles, California, during April 13-18, 1980.

C. E. ALBRIGHT is Assistant Professor, Department of Welding Engineering, Ohio State University, Columbus, Ohio.

vided by the steel. This pressure encourages welding.

3. Large interfacial shear is developed between the aluminum and the steel; this also encourages welding.

4. The aluminum, in deforming from a thick cylinder to a very thin sheet, increases in surface area several times. This increase in surface area causes cracking of the original oxide and exposes virgin metal.

Double Cantilever Beam Specimens

The specimen geometry which proved to be practical was the double cantilever beam (D.C.B.) or crack-line-loaded fracture toughness specimen. Notched bar specimens do not yield enough measurable strain during mechanical testing, and superimposed bending moments make fracture tests suspect. The work of Ripling (Ref. 8) was very helpful in the design of this type of D.C.B. specimens.

Figure 1 gives the dimensions of the final specimen design. Two bars of steel are welded together by forging a wire of pure aluminum between the two interior surfaces of the bars. The elastic design of the specimen was based on the assumption that the aluminum layer is so thin that it does not affect the elastic response of the specimen. The predicted elastic response of this specimen yields loads and displacements which are easily measurable for crack extension force at instability (G_{Ic}) values between 100 and 20,000 N/m (newtons per meter), i.e., 0.57 and 114.2 lbf/in.

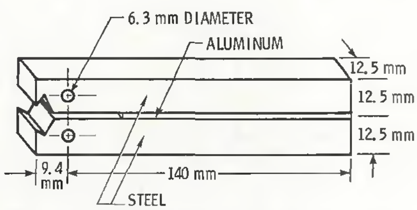

Fig. 1—Double cantilever beam specimen

Deformation Welding Specimen Preparation

The materials used in the fabrication of the D.C.B. specimens were AISI 4340 steel and 99.999% pure aluminum. The steel bars were machined from ¾ × ¾ in. (19 × 19 mm) bar stock, all from the same mill heat. The bars were rough machined, austenitized by heating to between 815 and 830°C (1499 to 1526°F) in a neutral salt bath, quenched in vigorously agitated oil and tempered for two hours at 550°C (1022°F) in a neutral salt bath. The final hardness of the bars was R_c 37 ± 2. The aluminum wire was swaged from a ¾ in. (19 mm) diameter aluminum rod. The final swaged diameter of the aluminum wire was 1.85 mm (0.07 in.).

After heat treating, the steel bars received a final grinding and the bar faying surfaces were lapped flat to within ±0.0025 mm (0.0001 in.). A 1.2 mm (0.05 in.) diameter, 0.13 mm (0.005 in.) deep, groove was milled the length of the center of the faying surface of one of the bars.

Fixturing and Assembly

After cleaning, the parts were stacked in a lateral restraining fixture in the following order:

1. The grooved bar with the faying surface up.
2. The aluminum wire, cut to approximately 125 mm (4.9 in.) in length, positioned in the groove with one end of the wire aligned with the end of the bar away from the pin loading holes.
3. The bar with the polyimide crack initiator placed on top of the wire with faying surface down.

The assembly was then wrapped in nickel foil and inserted into a stainless steel heat treating bag. The bag with assembly was placed in an argon atmosphere glove box and alternately evacuated to 1 torr and backfilled with argon. After 3 repetitions of evacuation and backfilling, the bag was sealed in the argon atmosphere by folding the bag approximately 12 mm (0.47 in.) from the open end three times and hammering the folds tight.

Welding in Hot Press

The assembly was then placed between the heated platens of a 50 ton capacity press. The temperature maintained during the hot press deformation welding cycle was 350 ± 7°C (662 ± 12°F). A force of 400 kN (45 tons) was applied so that the aluminum wire was forged over the steel faying surfaces and excess aluminum was extruded past the edge of the sample. The average compressive stress in the aluminum was 200 MPa (32,000 psi). The pressure was held for 15 minutes (min) and was then reduced to 44.5 kN (5 tons) while the platens and specimen assembly were allowed to cool to below 150°C (302°F).

Heat Treating

Each as-welded specimen to be heat treated was wrapped in tantalum foil and placed in a stainless steel heat treating bag. The bag then received the same sequence of evacuation and backfilling with argon and final fold sealing used to encapsulate specimens during welding. One specimen was obtained at each permutation of time and temperature in the matrix 360, 380, 400, 420, and 440°C (680, 716, 752, 788, and 824°F) and 0.5, 2, 8 and 32 hours (h).

Mechanical Testing

To achieve an accurate characterization of specimen compliance, the load displacement response of two specimens was measured at various simulated crack lengths. Values of G_c were then measured using a load reversal technique on an Instron universal testing machine. Details of the mechanical testing techniques and results are presented elsewhere (Ref. 9).

Table 1—G_{Ic} For Various Heat Treatments

Sample no.	Heat treatment[a]	G_{IC}(N/m)[a]	Failure type
DCB-10	Not heat treated	5709	Aluminum
DCB-24	360°C (680°F) for 0.5 h	6094	Aluminum
DCB-25	360°C (680°F) for 2.0 h	4746	Aluminum
DCB-26	360°C (680°F) for 8.0 h	5954	Aluminum
DCB-23	360°C (680°F) 32.0 h	2995	Aluminum and Interfacial[c]
DCB-22	280°C (536°F) for 0.5 h	8196	Aluminum
DCB-20	380°C (716°F) for 2.0 h	5884	Aluminum
DCB-19	380°C (716°F) for 8.0 h	708	Interfacial
DCB-21	380°C (716°F) for 32.0 h	471	Interfacial
DCB-29	400°C (752°F) for 0.5 h	4133	Aluminum and Interfacial[c]
DCB-30	400°C (752°F) for 2.0 h	1733	Aluminum and Interfacial[c]
DCB-28	400°C (752°F) for B.0 h	263	Interfacial
DCB-27	400°C (752°F) for 32.0 h	3.9[b]	Interfacial
DCB-17	420°C (788°F) for 0.5 h	560	Interfacial
DCB-16	420°C (788°F) for 2.0 h	856	Interfacial
DCB-18	420°C (788°F) for 8.0 h	806	Interfacial
DCB-15	420°C (788°F) for 32.0 h	66.2	Interfacial
DCB-12	440°C (824°F) for 0.5 h	1156	Interfacial
DCB-11	440°C (824°F) for 2.0 h	630	Interfacial
DCB-13	440°C (824°F) for 8.0 h	254	Interfacial

[a]Multiply by 1.355818 to convert to foot pound force

[b]Measurements made at crack length beyond 76.2 mm (3 in.)

[c]These specimens had regions of both aluminum and interfacial failures.

Fractography and Metallography

After toughness testing, a 25 mm (1 in.) long piece was cut from the uncracked end of the specimen. This end piece was saved for cross sectioning. The remaining 125 mm (4.9 in.) of specimen was wedge loaded to failure. The fracture surfaces were observed microscopically and photographed. The uncracked ends were mounted in clear epoxy resin, polished and etched.

On specimens where a reaction product layer was observed, the average layer thickness was measured. This measurement was performed by superimposing a grid of 19 lines on a 100 × 125 mm (3.9 × 4.9 in.) Polaroid® photomicrograph of the layer cross section. The layer thickness was thus measured where a grid line crossed the layer at right angles to the interface. These measurements were then averaged to obtain the average reaction product layer thickness. The measurement was made only on specimens with a continuous reaction product layer.

Aluminum Etch Metallography

On specimens that failed predominantly through the aluminum, cross section metallography proved to be an inadequate technique for proper observation of the reaction product. A technique by which the aluminum was dissolved from the fracture surface revealing the reaction product at the steel-aluminum interface was developed. This process dissolved the aluminum metal but left the aluminum-iron reaction products untouched. The segments were placed in a 10% KOH solution heated to approximately 70°C (158°F) and were then observed in the scanning electron microscope.

In an attempt to determine growth rates of the particles, the average largest diameter of reaction product particles observed on each specimen was measured. Since the number density of particles varied with distance from the center of the faying surface (transverse or width direction), this observation was only made 3 mm (0.12 in.) from the edge of the specimen or approximately half way between the center and edge of the specimen. Five ×2250 photomicrographs at random longitudinal positions were taken. The diameter of the 10 largest particles observed was measured. These diameters were averaged to obtain the estimate of average largest particle diameter.

Microprobe analysis was performed to determine approximate chemistries of significant fractographic features.

Results

The values of G_{Ic} show definite trends in both heat treating temperature and time—Table 1. The G_{Ic} values show a definite decreasing trend at 360, 380 and 400°C (680, 716 and 752°F). G_{Ic} values at 420 and 440°C (788 and 824°F) are much lower (an average of 572 N/m, i.e. 422 ft-lb, at 420°C and 680 N/m, i.e., 502 ft-lb, at 440°C) but do not seem to show a decreasing trend. Figure 2 is a plot of G_{Ic} vs. heat treating time at various heat treating temperatures.

It was clear, upon visual inspection of the fracture surfaces, that two distinct types of failures were occurring. The first type of failure yielded two identical fracture surfaces appearing as dull silver. It was clear that failure was occurring through the aluminum. These aluminum failures average 6097 N/m (4497 ft-lb) in G_{Ic}.

The second type of failure yielded two completely different appearing fracture surfaces; one surface appeared silver though dull and flatter than type 1 fracture surfaces, while the other surface appeared battleship gray. It was clear that these failures occurred at the weld interface. These interfacial failures average 525 N/m (387 ft-lb) in G_{Ic}.

Three specimens appeared to have fracture surfaces comprised of mixed areas of aluminum and interfacial failures. Two specimens, DCB-23 and DCB-29, had G_{Ic} values of 2995 N/m (2209 ft-lb) and 4133 N/m (3848 ft-lb) respectively, values intermediate between the aluminum and interfacial failure averages.

Specimen DCB-30, though failing predominantly at the interface, did show a mixture of aluminum and interfacial fracture behavior. G_{Ic} for specimen DCB-30 was 1733 N/m (1278 ft-lb); low, but still intermediate between the aluminum and interfacial failure average. Table 1 includes the observed failure type for each specimen. One typical specimen fracture surface (DCB-27) was subjected to x-ray crystallographic analysis. The full width of a typical aluminum failure is shown in Fig. 3.

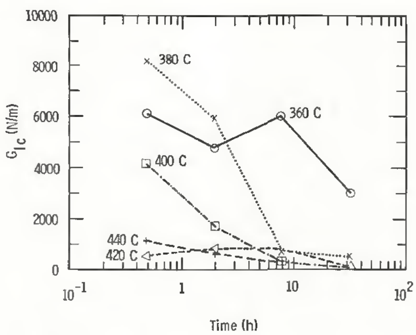

Fig. 2—G_{Ic} vs. time at various heat treating temperatures

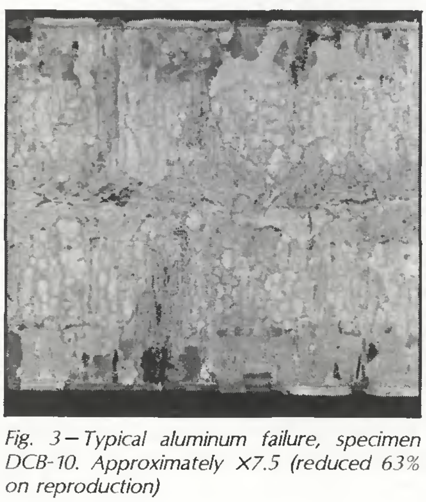
Fig. 3—Typical aluminum failure, specimen DCB-10. Approximately ×7.5 (reduced 63% on reproduction)

Three distinct zones were observed on the fracture surfaces in the width or transverse direction: a central zone, an edge zone, and a zone midway between the center and the edge of the specimen—Fig. 3. In every case, the fracture surfaces did show differences among the three zones.

The center zone varied in width between 0.5 and 1.0 mm (0.02 and 0.04 in.) on either side of the center line of the faying surface. The edge zone varied in width between 0.2 and 2.0 mm (0.008 and 0.08 in.) from the edge of the specimen. The midzone comprised the area between the center and edge zones and varied between 9.7 and 12.0 mm (0.38 and 0.47 in.) in width. Since the midzone clearly dominated the specimen in fraction of fracture surface (between 76 and 94%) unless otherwise stated, all fracture surface observations and future analysis concern the midzone.

The predominant feature of the midzone is the array of pits or depressions separated by peaked walls. A typical scanning electron fractographs at ×100 is shown in Fig. 4. In this fractograph, the depressions are shown in more detail, and the walls of the depressions appear to be composed of jagged steps.

The fracture surfaces of interfacial failures were strikingly different. Failure indeed occurred at some plane close to the interface between the aluminum and the steel. For ease of identification, the aluminum side refers to the fracture surface closer to the aluminum layer, and the steel side refers to the surface closer to the steel bar. Figure 5 shows a typical interfacial fracture surface in full width. The light areas are the aluminum side, the darker areas are the steel side.

Figure 6 gives higher magnification fractographs of the aluminum side frac-

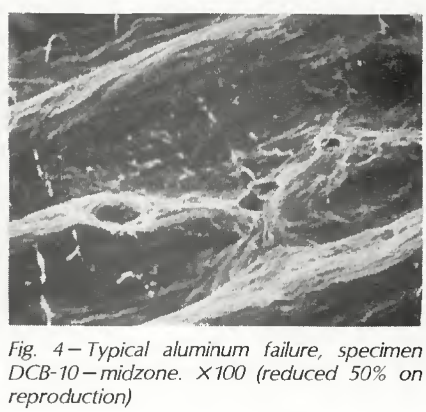
Fig. 4—Typical aluminum failure, specimen DCB-10—midzone. ×100 (reduced 50% on reproduction)

Fig. 5(above) — Typical interfacial failure — aluminum side in the light areas and steel side in the dark areas — specimen DCB-13. Approximately X7.5 (reduced 50% on reproduction)

Fig. 6(right) — Aluminum side of specimen DCB-17 fracture surface: A — rectangular voids; B — rounded voids. X6000 (reduced 35% on reproduction)

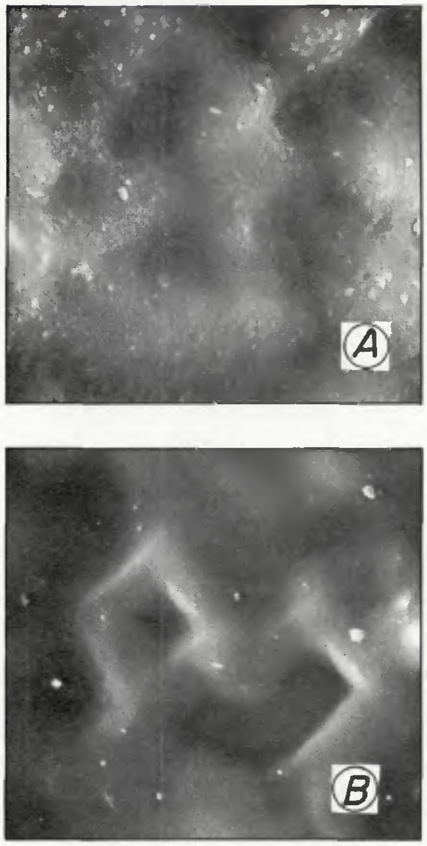

ture surface of Specimen DCB-17. It is clearly shown in Fig. 8 that void geometry included rectangular and rounded pits on the same specimen. At X6000 magnification the void walls appear quite smooth and lacking in detail except for fine particulate contamination.

Metallography

Cross Section Metallography

The cross section metallography revealed more difference between aluminum and interfacial failures. The cross sections of the as-welded specimens revealed a continuous, straight interface between the aluminum and the steel with no sign of a reaction product — Fig. 7. Interfacial failure specimens revealed a reaction product layer growing into the aluminum layer — Fig. 8.

The measurements of the average reaction product layer thickness are given in Table 2. The measurement was made only on specimens with a continuous reaction product layer in the midzone.

The reaction product layer was not continuous on specimens which showed a combination of aluminum and interfacial fracture behavior. Figure 9 shows typical examples of this intermittent reaction product layer.

These specimens were helpful in determining the relationship of the reaction product to the original steel-aluminum interface. The particles appear to extend approximately five times further into the aluminum than into the steel. The particles are roughly hemispherical in shape, i.e., altitudes are approximately half the base diameter. Figure 9 shows these features.

Aluminum Etch Metallography

The aluminum etch metallography experiment yielded significant information on the formation and growth of the reaction product. After dissolving the aluminum that remained on aluminum fracture surfaces, mound shaped particles were observed adhering to the steel and growing into the aluminum. The location of the particles was not random; the particles tended to locate along straight line bands — Fig. 10. The number density of particles also tended to be higher toward the edge zone and decrease toward the central zone.

The particles tended to increase in size with both increasing temperature and time. One specimen (with very small particles) showed quite a bit of damage and loss of particles after etching. Although many particles are missing, the pits in the steel give an excellent record of the particle diameters and locations.

Figure 11 gives an arrangement of photomicrographs of particles observed at 360, 380 and 400°C (680, 716 and 752°F) for all of the heat-treating times; the formation and growth of particles both with respect to temperature and time are clearly seen.

The average largest particle diameters as a function of heating treating time and temperature are given in Table 3.

Microprobe and X-Ray Analysis

The microprobe was very useful in the approximate chemical analysis of fracture surfaces. Microprobe analysis showed that aluminum failures gave two fracture surfaces of essentially pure aluminum. As was expected, failure was occurring within the aluminum layer.

The microprobe analysis of interfacial failures showed that the aluminum side of the fracture surface was essentially pure aluminum with no detectable iron. The steel side of the fracture surface was a mixture of iron and aluminum.

X-ray crystallographic examination of the steel side of specimen DCB-27 resolved only two crystal structures, the iron-aluminum intermetallic compound Fe_2Al_5 and iron. The ratio of x-ray peak intensities was close to ideal for the two crystal structures.

This evidence, along with the fractography, demonstrates that interfacial failure occurs between the intermetallic layer and the porous aluminum layer.

Discussion

Interfacial Observations

Aluminum Fracture Surfaces. As previously stated, microprobe analysis of the fracture surfaces shows that failure occurs through the aluminum layer. Aluminum fracture surfaces are characterized by midzones having pits or voids — Figs. 3 and 4. These observations are consistent with the void coalescence theory of ductile rupture (Ref. 10, 11). According to the theory, voids nucleate around inclusions and grow under the

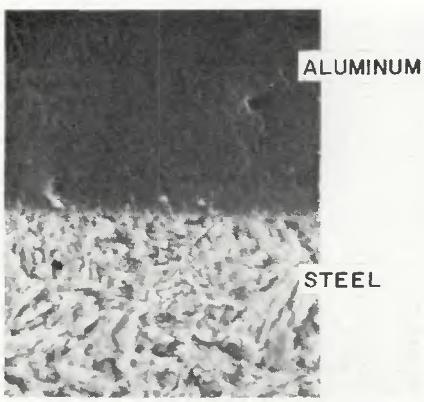

Fig. 7 — Typical cross section at the steel-aluminum interface of an aluminum failure, specimen DCB-10. X3000 (reduced 60% on reproduction)

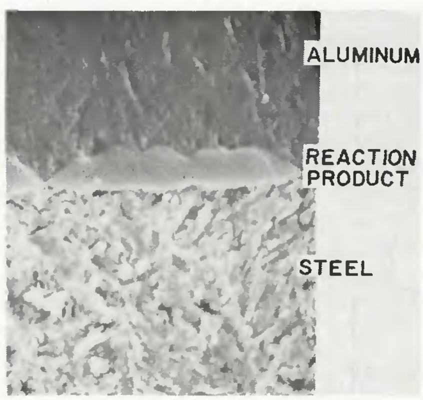

Fig. 8 — Typical cross section at the steel-aluminum interface of an interfacial failure, specimen DCB-19. X3000 (reduced 60% on reproduction)

Table 2—Average Reaction Product Layer Thickness as a Function of Heat Treatment

Specimen no.	Heat treatment	Thickness, μm)[a]	
DCB-19	380°C for 8.0 h	2.55	2.27 avg.
DCB-21	380°C for 32.0 h	1.99	
DCB-28	400°C for 8.0 h	2.87	3.06 avg.
DCB-27	400°C for 32.0 h	3.24	
DCB-17	420°C for 0.5 h	2.62	
DCB-16	420°C for 2.0 h	2.06	2.08 avg.
DCB-18	420°C for 8.0 h	1.65	
DCB-15	420°C for 32.0 h	1.99	
DCB-12	440°C for 0.5 h	3.26	2.44 avg.
DCB-11	440°C for 2.0 h	1.94	
DCB-13	440°C for 8.0 h	2.13	

[a] Average thickness — 2.39 μm; mean deviation — 0.525

Table 3—Average Diameter of 10 Largest Particles Observed on Each Specimen as a Function of Heat Treatment

Specimen no.	Heat treatment	Diameter, μm
DCB-24	360°C for 0.5 h	1.58
DCB-25	360°C for 2.0 h	1.88
DCB-26	360°C for 8.0 h	1.94
DCB-23	360°C for 32.0 h	5.60
DCB-22	380°C for 0.5 h	2.22
DCB-20	380°C for 2.0 h	3.64
DCB-19	380°C for 8.0 h	7.96
DCB-29	400°C for 0.5 h	2.93
DCB-30	400°C for 2.0 h	5.82

influence of the triaxial tensile stress conditions existing in front of a propagating crack. The voids grow until they intersect, their walls failing by plastic instability or necking. Since the 99.999% pure aluminum has an extremely low inclusion density, very few sites for void nucleation exist, and thus a few voids grow and intersect at very large diameters. This effect of inclusion density on void size has been observed (Ref. 11, 12, 13).

Interfacial Fracture Surfaces and Interfacial Reactions. Careful observations made on interfacial fracture surfaces lead to the conclusion that ductile rupture is not the mechanism responsible for interfacial failure. The pits or voids appearing on the aluminum side of interfacial fracture surfaces (Figs. 6 and 12) are much different in appearance than the voids or

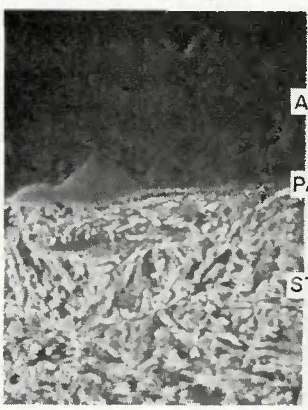

Fig. 9 — Two individual reaction product particles at the aluminum interface

pits formed in the ductile rupture process (Figs. 3 and 4). The voids on interfacial fracture surfaces do not have sharp crests or peaks on the wells between the voids which would indicate plastic instability or necking. Instead, these void intersections are smooth and rounded. There are no commonly observed fracture details (slip line, ductile dimples, cleavage facets, etc.), on interfacial fracture surfaces (Ref. 14).

A comparison of Figs. 12 and 13 shows that the total volume of voids in the aluminum is of the same order of magnitude as the volume of intermetallic phase. The general geometry of the voids varied from rounded to rectangular with position on the fracture surface.

The voids appearing on the aluminum side of interfacial fracture surfaces are formed by the condensation of vacancies produced by the interdiffusion process. Before this can be shown, observations on the products of the iron-aluminum reaction and the interdiffusion process must be discussed.

The steel side of interfacial fracture surfaces is saturated with dome-shaped particles of Fe_2Al_5 — Fig. 13. This fact is supported by cross section metallography (Figs. 8 and 9), x-ray crystallographic analysis and microprobe analysis. The aluminum etch metallography shows that individual particles nucleate and grow into a continuous layer with increasing temperature and time at 360, 380 and 400°C (680, 716 and 752°F) — Figs. 10 and 11. Contrary to the reporting by other authors of only continuous layers

Fig. 10 — Mound shaped particles adhering to the steel surface after dissolving the aluminum specimen DCB-29. X2250 (reduced 60% on reproduction)

(Ref. 6, 15), the reaction proceeds by a process of nucleation and growth of individual particles of Fe_2Al_5. Nucleation does not seem to be random. Figure 10 shows that particles tend to cluster and form along straight lines, indicating preferential nucleation sites. Thus, it is difficult to characterize the nucleation event.

De Hoff (Ref. 16) discussed methods of estimating nucleation and growth rates from particle dimension distributions. It can be assumed that the largest particles observed on any particular specimen must nucleate at the shortest nucleation time. By measuring only the largest particles on each specimen, the nucleation time can be assumed constant at any given temperature. A measurement of the diameters of the largest particles observed as a function of time at a given temperature will thus show the increase in particle diameter with time, and a particle growth rate can be determined.

The growth of particles at a given temperature is very important because it is directly related to the interdiffusion process. By the extension of Kidson's (Ref. 17) model of multiple phase interdiffusion, the growth of particles can be represented by:

$$D = A(T)\sqrt{t} \tag{1}$$

where D = particle diameter, t = time, and A(T) = a constant dependent on temperature.

By assuming the nucleation time for the first particles to nucleate to be small compared to heat treating times, the largest particle diameter data of Table 3 is least-squares fitted to the relationship given in equation (1). This method allows A(T) to be determined at 360, 380 and 400°C (680, 716 and 752°F).

Figure 14 shows the derived growth functions compared to the largest particle diameter data. If the time, t, is in hours and particle diameter, D, is in micrometers, the derived A(T) values are:

$$A(360°C) = 1.31\,\frac{\mu m}{\sqrt{hr}} \tag{2}$$

$$A(380°C) = 2.85\,\frac{\mu m}{\sqrt{hr}} \tag{3}$$

$$A(400°C) = 4.12\,\frac{\mu m}{\sqrt{hr}} \tag{4}$$

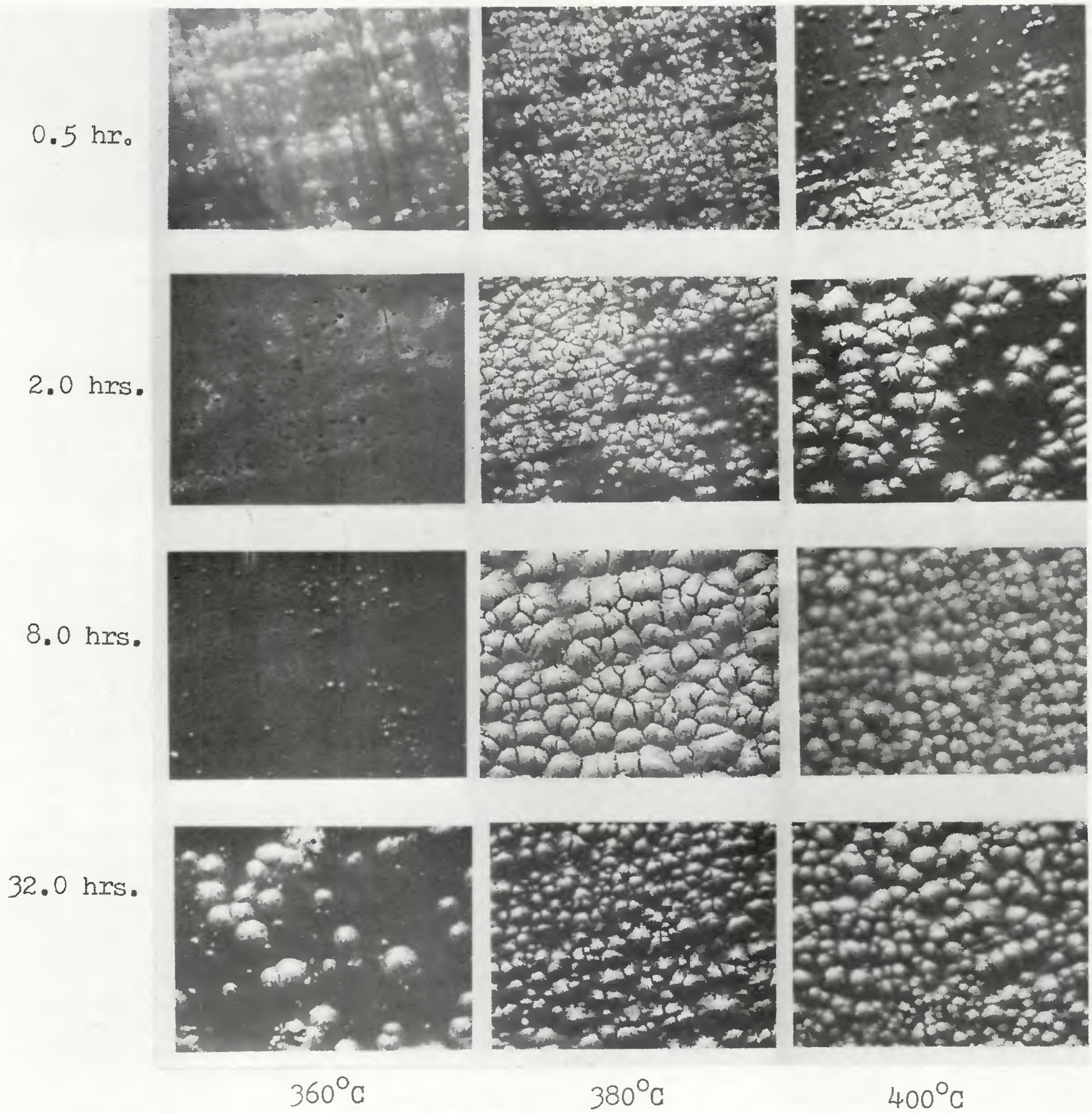

Fig. 11 — Reaction product particles as a function of heat treating time and temperature. ×2250

The literature on interdiffusion between aluminum and steel was in a state of confusion until very recently. Workers have reported various temperatures for the effective start of interdiffusion over a vast range of 350 to 600°C (662 to 1112°F) (Ref. 18). The recent work of Bedford (Ref. 19) shows that interdiffusion is greatly suppressed by high concentrations of oxygen in the steel. A highly deoxidized steel (the oxygen concentration was only 0.0008% by weight) was used in the present study, which explains the relatively high interdiffusion rates at these temperatures.

Relationship Between Interfacial Structure and Specimen Toughness

The basic experimental observations can be expressed in terms of three generalities:

1. The fracture process changes from ductile rupture to interfacial separation with increasing temperature and time.
2. G_{Ic} values change from an average of 6097 N/m (210 lbf/in.) to an average of 525 N/m (18.1 lbf/in.) with increasing temperature and time.
3. The structure of the interface changes from a continuous aluminum-steel interface to an interface containing Fe_2Al_5 layer and void layer in the aluminum with increasing temperature and time.

It is shown that the toughness of the steel-aluminum interface is a direct function of the interfacial structure, and that the interdiffusion process causes the interfacial structural changes.

The causal link in relating the interdiffusion process to the decrease in toughness is the formation of vacancy condensation voids in the aluminum adjacent to the Fe_2Al_5 layer. Thus, the discussion is returned to the formation and growth of vacancy condensation voids.

There is a 2.6% volume shrinkage associated with the reaction of aluminum and iron to form Fe_2Al_5 (Ref. 10, 11). Since it is apparent that the void volume is about the same order of magnitude as the volume of Fe_2Al_5 (Figs. 13 and 14), the reaction shrinkage cannot account for the much larger volume of voids formed in the aluminum.

The shrinkage cannot be causing complete separation between the aluminum and the Fe_2Al_5. Such separation would cause the aluminum to replicate the surface of the intermetallic. From Figs. 13 and 14, it is seen that the aluminum voids bear no resemblance to the matching Fe_2Al_5 surfaces.

The facts that interdiffusion can cause an excess population of vacancies (Kirkendall effect — Ref. 20, 21) and that a supersaturation of vacancies can coalesce into voids (Ref. 22, 23) are well documented. Void formation is common in interdiffusion couples (Ref. 21, 24). Vacancy condensation voids in aluminum can take a number of forms including the octahedron which explains the rectangular appearance of some of the voids in Figs. 6 and 12 (Ref. 22). Thus vacancy condensation into voids accounts for the porosity of the aluminum adjacent to the Fe_2Al_5. Similar porosity was observed by Ludemann (Ref. 15) after pressure welding aluminum to steel.

The porosity causes essentially complete separation between the aluminum and the Fe_2Al_5 layer. This separation correlates well with the following observations:

1. There is a lack of any fractographic detail on the midzones of interfacial fracture surfaces indicative of a commonly observed fracture process (ductile rupture, cleavage, intergranular failures, etc.).

2. The growth of the intermetallic layer is stopped (see Table 2). Within experimental error, the thickness of the Fe_2Al_5 layer does not change with temperature or time on specimens exhibiting interfacial failure.

3. The toughness of interfacial failure is extremely low. Ductile rupture through the aluminum layer is observed in the center zone of interfacial failure. The value of G_{Ic} for ductile rupture in the center zones should be the same as G_{Ic} for aluminum failure, since both failures occur by the same process. Thus, the toughness of the center zone accounts for all of the residual toughness of interfacial failures; the toughness of the midzones is essentially zero.

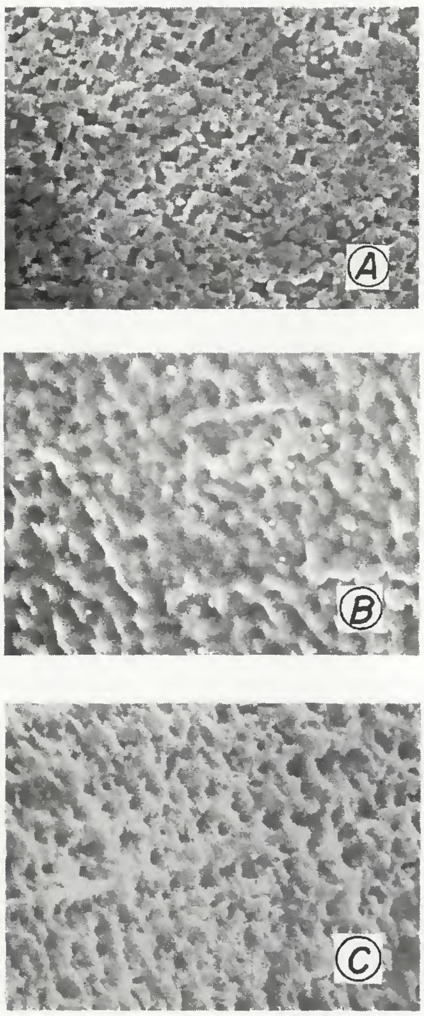

Fig. 12 — Interfacial failures on aluminum side of three specimens: A — DCB-16; B — DCB-17; C — DCB-13. ×1000 (reduced 60% on reproduction)

The volume of aluminum needed to form the Fe_2Al_5 (165 Å^3) is 80% of the Fe_2Al_5 volume (206.5 Å^3). This volume of aluminum must cross the aluminum-Fe_2Al_5 interface by a diffusion process. Since iron diffusion into the aluminum is very low (no iron was detected with microprobe analysis), then the Kirkendal Equation (Ref. 20, 21) demands that the flux of vacancies into the aluminum must be close in magnitude to the flux of aluminum atoms into the Fe_2Al_5. If a high percentage of these vacancies condense into voids, the void volume would be of the same order of magnitude as the Fe_2Al_5 volume.

Ludemann (Ref. 15) observed porosity forming in the aluminum close to the intermetallic layer, but failure in his experiment was by brittle failure through the intermetallic layer. Interdiffusion in this case occurred during the pressure welding process under high hydrostatic compressive stresses. Under these conditions it is to be expected that the aluminum would be forced back into contact with the intermetallic layers and the separation would not occur.

It is thus concluded that the decrease in toughness is the direct result of interdiffusion producing a void layer which in turn causes separation between the Fe_2Al_5 and the aluminum.

Since interfacial failure is the final result of interdiffusion, G_{Ic} must show a transition from the aluminum failure average to the interfacial failure average with increasing interdiffusion. The extent to which individual particles have grown is directly related to the amount of interdiffusion that has occurred. Figure 15 is a plot of G_{Ic} vs. the largest particle data of Table 3. As expected, a transition from the aluminum average G_{Ic} to the interfacial average G_{Ic} occurs in the particle diameter range from 4 to 8 microns.

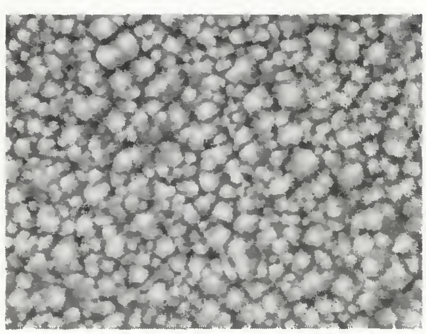

Fig. 13 — Typical interfacial failure, steel side, specimen DCB-16. ×1000

In equation 1, particle diameter is related to temperature through the parameter A(T). Although it is clear that particle growth stops with the onset of interfacial failure, extrapolations to larger diameters show that specimens should exhibit interfacial failure toughness. Figure 16 is a plot of G_{Ic} vs. particle diameter calculated by using Equation 1 and the previously obtained A(T) values. Again, Fig. 16 shows the transition from aluminum to interfacial G_{Ic} values occurs between 4 and 8 microns.

Conclusion

In past studies joint embrittlement has been associated with a critical thickness of the intermetallic layer. In this study, three general observations are made:

1. A transition from ductile rupture through the aluminum to failure at the steel aluminum interface occurs with increasing heat treating time at 360, 380 and 400°C (680, 716 and 752°F). The transition occurs at shorter times as temperature is increased.

2. Failure through the aluminum exhibited relatively high values of G_{Ic} (6097 N/m, i.e., 210 lbf/in.) while interfacial failures exhibited low values of G_{Ic} (525 N/m, i.e., 18.1 lbf/in.). Three specimens failed by a mixture of aluminum and interfacial failures, with failure occurring through the aluminum layer in some areas, and at the steel-aluminum interface in other areas. These specimens exhibited G_{Ic} values between the aluminum and interfacial averages.

3. A reaction product of Fe_2Al_5 is observed to nucleate as distinct particles which grow and intersect with time to form a continuous layer at the steel-aluminum interface. Particle growth rate is proportional to the square root of time. Voids form in the aluminum adjacent to the Fe_2Al_5. Growth of the Fe_2Al_5 layer stops on specimens exhibiting interfacial failure.

These observations are consistent when viewed in terms of interdiffusion theory. An imbalance in the interdiffusion rates of individual atomic species creates a flux of vacancies which condense into voids in the aluminum adjacent to the Fe_2Al_5. The void layer grows with the

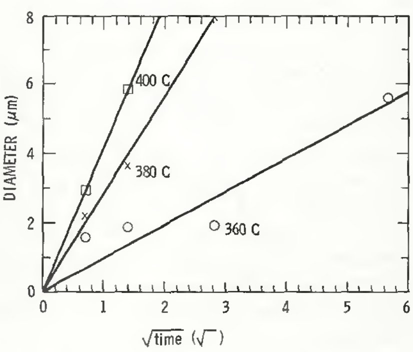

Fig. 14 — Average largest particle diameter vs. square root of time

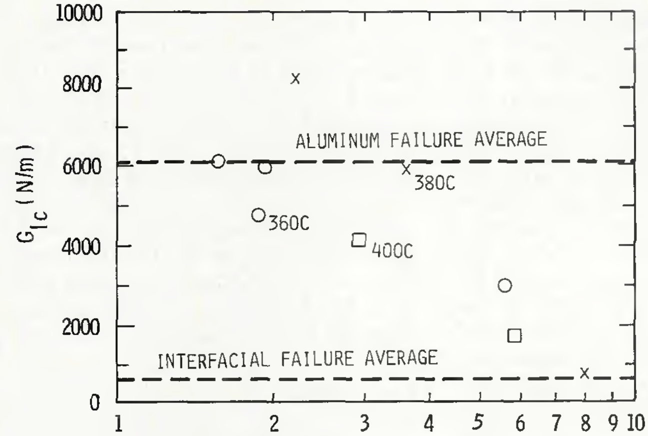

Fig. 15 — G_{Ic} vs. measured average largest particle diameter

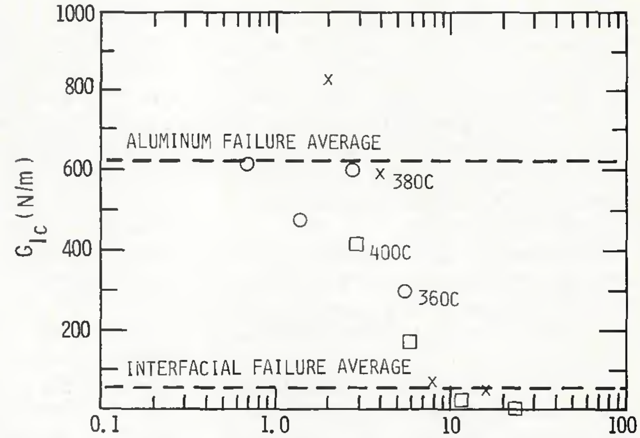

Fig. 16 — G_{Ic} vs. particle diameter calculated from D = A(T) t

growth of the Fe_2Al_5. The end result of this process is separation between the aluminum layer and the Fe_2Al_5 layer. This separation explains the stoppage of intermetallic layer growth on specimens exhibiting interfacial failure.

The interdiffusion with intermetallic layer growth model of Kidson (Ref. 9) is extended to present the growth rate of hemispherical particles. Particle diameter, a parameter which is shown to be characteristic of the amount of interdiffusion that has occurred, can be written as:

$$D = A(T)\sqrt{t} \quad (1)$$

where D = particle diameter, t = time, and A(T) = temperature dependent term

When G_{Ic} is plotted vs. the largest particle diameter estimated for each specimen, a transition in toughness is observed. Toughness values drop from G_{Ic} average for aluminum failure to the G_{Ic} average for interfacial failure when the estimated largest particle diameter increases from 4 to 8 microns, demonstrating the relationship between toughness and interdiffusion.

The relationship between toughness and intermetallic particle size establishes the temperature and time limits for joint service. Joint embrittlement can be avoided by preventing particles of Fe_2Al_5 from growing beyond 4 μm in diameter at the steel-aluminum interface. Figure 14 gives the temperature and times which must not be exceeded if particles are to be kept below 4 μm in diameter.

Within these temperature and time limitations, deformation weldments between steel and aluminum can be used in engineering structures without failure due to interfacial embrittlement. It must be emphasized that steel-aluminum weldments will be extremely susceptible to galvanic corrosion attack, and great care must be taken to prevent galvanic corrosion of the weldments in engineering structures.

The fabrication and experimental techniques developed in this study may be applied to many composite systems other than the steel-aluminum composite system. Relatively high strengths are required for prospective bar materials, and relatively low strength and high ductility are required for the materials to be plastically deformed. By imaginative uses of platings and coatings, these mechanical requirements could be met. The toughness of these other dissimilar metal solid phase welded composite systems is an interesting area for future study.

Acknowledgment

The project described in this paper was supported by Sandia Corporation, Albuquerque, New Mexico, with funds and facilities support.

References

1. Fellom, R., ed. 1977. Global report aluminum 1977. *Light Metal Age*, April: 5-8.
2. Fellom, R., ed. 1977. 114 lbs. aluminum seen on 1978 cars. *Light Metal Age*, April: 32.
3. Patee, H. E. 1968. Joining aluminum to steel. *Light Metal Age*, June: 18-23.
4. Evans, Ulick R. 1966. *The corrosion and oxidation of metals*: 187-207. New York: St. Martin's Press, Inc.
5. Kuber, B. 1970. Welding and brazing joints between aluminum and steel alloys. *Aluminum* 46 (4): 304-310 (in German).
6. McEwan, K. J. B., and Milner, D. R. 1962. Pressure welding of dissimilar metals. *British Welding Journal*, July: 406-420.
7. Mostovoy, S., and Ripling, E. J. 1966. Fracture toughness of an epoxy system. *Journal of Applied Polymer Science* 10: 1351-1371.
8. Ripling, E. J.; Mostovoy, S.; and Patrick, R. L. 1964. Measuring fracture toughness of adhesive joints. *Materials Research and Standards*, March: 129-134.
9. Albright, C. E. The fracture toughness testing of steel-aluminum deformation joints. To be published.
10. Gurland, J., and Plateau, J. 1963. The mechanism of ductile rupture of metals containing inclusions. *Trans. of the ASM*, 56: 442-454.
11. Beachem, C. D., and Meyn, D. A. 1968. Fracture by microscopic plastic deformation process. *Electron Fractography*, A.S.T. S.T. P. 436: 59-88.
12. Edelson, B. I., and Baldwin, W. M. Jr. 1962. The effect of second phases on the mechanical properties of alloys. *Trans. of the ASM*, 55: 230-250.
13. Broek, D. 1973. The role of inclusions in ductile fracture and fracture toughness. *Engn. Fracture Mechanics*, 5: 55-66.
14. American Society for Metals Handbook Committee. 1974. Fractography and atlas of fractographs. *Metals handbook*. 8th ed., vol. 9. Metals Park: American Society for Metals.
15. Ludemann, W. D. 1969. A fundamental study of the pressure welding of dissimilar metals through oxide layers. Report UCRL-50744.
16. DeHoff, R. T. 1971. The analysis of the evolution of particle size distribution during microstructural change. *Metallurgical Transactions* vol. 2, Feb.: 522-526.
17. Kidson, G. V. 1961. Some aspects of the growth of diffusion layers in binary systems. *Journal of Nuclear Materials* 3 (1): 21-29.
18. Makunin, M. S.; Zheladnov, V. I.; and Arzhanyi, P. M. 1973. The reaction of aluminum and iron in the solid state. *Doklady Akademii Nauk SSSR* 212 (3) (in Russian) translated in *Academy of Sciences of the USSR, Proceedings*, phys. chem., vol. 212: 800-802.
19. Bedford, G. M., and Boustead, J. 1978. The influence of oxygen and nitrogen on the growth of intermediate phases during bonding of iron to aluminum. *Journal of Materials Science* 13: 253-260.
20. Smigelskas, A. D., and Kirkendall, E. D. 1946. Zinc diffusion in alpha brass. *Trans. AIME*, vol. 171: 130-142.
21. da Silva, L. C. C., and Mehl, R. F. 1951. Interface and marker movements in diffusion in solid solutions of metals. *Trans. AIME*, vol. 191, Feb.: 155-173.
22. Kiritani, M.; Yoshiharu, V.; and Yoshida, S. 1964. Shape of voids in quenched aluminum. *Journal of the Phys. Soc. of Japan* 19 (9).
23. Yoshida, S.; Kiritani, M.; Shiumura, Y.; and Yoshinaka, A. 1965. Voids in quenched gold. 1965. Journal of the Phys. Soc. of Japan 20: 628-629.
24. Seith, W., and Heumann, T. 1955. *Diffusion of metals: exchange reactions*. Translation series, AEC-TR-4506: 132-141. United States Atomic Energy Commision, Division of Technical Information.
25. Wagner, C. as cited in Jost, W. 1952 (revised 1960). *Diffusion in solids, liquids, and gases*: 72. New York: Academic Press.